This is an open access article published under an ACS AuthorChoice License, which permits copying and redistribution of the article or any adaptations for non-commercial purposes.

ACS NANO

Cite This: ACS Nano 2018, 12, 8467−8476

www.acsnano.org

ARTICLE

In Situ Observation of Atomic Redistribution in Alloying Gold−Silver Nanorods

Jessi E. S. van der Hoeven,[†,‡] Tom A. J. Welling,[‡] Tiago A. G. Silva,[§] Jeroen E. van den Reijen,[†] Camille La Fontaine,[∥] Xavier Carrier,[§] Catherine Louis,[§] Alfons van Blaaderen,[*,‡] and Petra E. de Jongh[*,†]

[†]Inorganic Chemistry and Catalysis, Debye Institute for Nanomaterials Science, Utrecht University, Universiteitsweg 99, 3584 CG Utrecht, The Netherlands

[‡]Soft Condensed Matter, Debye Institute for Nanomaterials Science, Utrecht University, Princetonplein 5, 3584 CC Utrecht, The Netherlands

[§]Laboratoire de Réactivité de Surface, Sorbonne Université, CNRS, F-75005, Paris, France

[∥]L'Orme des Merisiers, Synchrotron SOLEIL, BP 48, Saint-Aubin, 91 192 Gif-sur-Yvette, France

Supporting Information

ABSTRACT: **The catalytic performance and optical properties of bimetallic nanoparticles critically depend on the atomic distribution of the two metals in the nanoparticles. However, at elevated temperatures, during light-induced heating, or during catalysis, atomic redistribution can occur. Measuring such metal redistribution *in situ* is challenging, and a single experimental technique does not suffice. Furthermore, the availability of a well-defined nanoparticle system has been an obstacle for a systematic investigation of the key factors governing the atomic redistribution. In this study, we follow metal redistribution in precisely tunable, single-crystalline Au-core, Ag-shell nanorods *in situ*, both at a single particle and an ensemble-averaged level, by combining *in situ* transmission electron spectroscopy with *in situ* extended X-ray absorption fine structure validated by *ex situ* measurements. We show that the kinetics of atomic redistribution in Au−Ag nanoparticles depend on the metal composition and particle volume, such that a higher Ag content or a larger particle size led to significantly slower metal redistribution. We developed a simple theoretical model based on Fick's first law that can correctly predict the composition- and size-dependent alloying behavior in Au−Ag nanoparticles, as observed experimentally.**

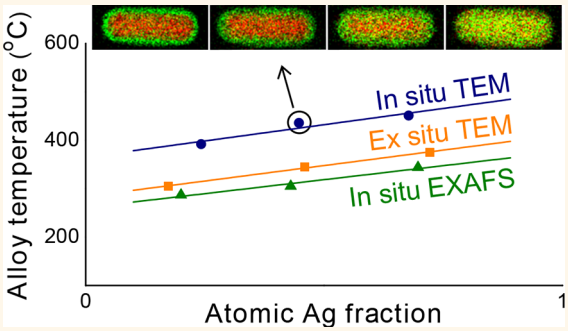

KEYWORDS: *alloying, bimetallics, in situ electron microscopy, in situ EXAFS, modeling*

By the combination of two metals in bimetallic nanoparticles (NPs), new and enhanced optical and catalytic properties can arise that can lead to applications in, *e.g.*, sensing, biomedicine, data storage, and catalysis.[1−10] The physicochemical properties of these bimetallic particles can be tuned not only by varying the metal composition but also by changing the atomic distribution of the two metals within the nanoparticles at a fixed composition (for example from core−shell to alloyed NPs).[8,10−15] The exact atomic distribution of the metals is particularly important in catalysis, in which the atoms close to the surface play a dominant role in the catalytic performance.[7,16−19] Furthermore, when exposing bimetallic nanoparticles to various gas atmospheres and heating them to elevated temperatures, atomic redistribution can occur.[11,17,18,20−26] This alters the optical[8,13,26] and catalytic properties[16−18,24,27] and can even lead to severe deactivation of the catalyst. Therefore, understanding atomic restructuring is crucial in the design of new catalytic and optical bimetallic materials.

Various techniques have been employed to follow metal redistribution *in situ*, each providing information on a different length scale.[20] Single-particle studies often make use of *in situ* transmission electron microscopy (TEM). With this technique, sub-nanometer or even atomic resolutions can be obtained while heating the sample.[17,21,22] This technique, however, is limited to samples that are very stable under electron irradiation to avoid electron-beam-induced artifacts.[28−30] Therefore, to verify the influence of the electron beam, it is important to also perform *ex situ* heating measurements.[30] Alternatively, X-ray-based techniques, such as X-ray photo-

Received: May 26, 2018
Accepted: July 11, 2018
Published: July 16, 2018

Downloaded via UTRECHT UNIV on April 11, 2019 at 09:31:50 (UTC).
See https://pubs.acs.org/sharingguidelines for options on how to legitimately share published articles.

© 2018 American Chemical Society

DOI: 10.1021/acsnano.8b03978
ACS Nano 2018, 12, 8467−8476

electron spectroscopy (XPS) and X-ray absorption fine structure (XAFS), also offer atomic information but averaged over a much larger number of particles.[18,25,31] XPS allows us to specifically study the surface composition of the NPs, and it is thus particularly suitable to measure surface segregation effects.[17,23,24] However, XAFS measurements give insight in the degree of mixing and oxidation state of the atoms within the nanoparticles and can be carried out in different gas atmospheres.[18,25,31] Thus, to follow the metal redistribution in bimetallic nanoparticles at multiple length scales (on an atomic, single-particle, and ensemble-averaged level), one technique does not suffice, and a multi-technique approach is required.

In addition, a systematic, quantitative, and reproducible study of atomic restructuring requires a well-defined model system. The use of rather heterogeneous bimetallic catalysts, obtained via standard catalyst preparation methods, is especially problematic when using techniques such as XAFS and XPS, in which the measured signal is an ensemble average. Therefore, the influence of fundamental parameters such as the metal composition and particle volume on the atomic redistribution process in bimetallic nanoparticles are largely unexplored.

In this study, we investigated the thermally driven atomic redistribution in single crystalline Au−Ag core−shell nanorods *in situ* both on a single particle and an ensemble-averaged level. We employed colloidally synthesized Au-core, Ag-shell nanorods of which the composition, size, and shape was tuned precisely.[9] By the coating of the metal nanorods with a protective mesoporous silica coating,[32] preservation of the particle shape during atomic redistribution was ensured.[8] We specifically chose a Au−Ag-based system because alloy formation is thermodynamically favorable at all compositions and the lattice spacings of Au and Ag closely match.[33] Because the nanorods are single-crystalline, this model system is well-suited to specifically study the kinetics of metal redistribution during alloying. To this end, we performed both *in situ* TEM and *in situ* EXAFS measurements, yielding sub-nanometer, single-particle and atomic, ensemble-averaged information, respectively. In addition, we validated the *in situ* measurements with *ex situ* measurements carried out in the absence of an electron or X-ray beam. In particular, we addressed the influence of the metal composition (Au−Ag ratio) on the alloying temperature of the Au-core, Ag-shell nanorods. We unambiguously showed the influence of the metal composition on the kinetics of the alloying process. Increasing Ag content led to slower metal redistribution, a trend that is opposite to the dependence of the melting temperature on the Au−Ag ratio. In addition, indications for size-dependent alloying were found where a decrease in particle volume led to lower alloying temperatures. We developed a simple theoretical model that correctly predicts the temperatures and time scales for metal redistribution as a function of particle volume and composition. Our study not only demonstrates a general, multiscale approach to monitoring metal redistribution in bimetallic nanoparticles but also reveals the influence of fundamental parameters governing metal redistribution, which is of importance in bimetallic nanoparticle applications.

RESULTS AND DISCUSSION

Preparation of Core−Shell Nanorods. Mesoporous silica-coated Au-core, Ag-shell nanorods (Au@Ag@SiO_2 NRs) with similar volumes but with three different Au-to-Ag ratios were colloidally synthesized. The colloidal synthesis was performed on a relatively large (milligram) scale to obtain the required amount of sample needed for the EXAFS measurements. To this end, the Ag-shell growth as described by Deng et al., comprising the reduction of Ag^+ ions on the Au nanorods by ascorbic acid, was performed in an acidified, instead of neutral, aqueous solution.[9] The presence of H^+ ions slowed the Ag-shell growth down considerably (from seconds to minutes), resulting in sufficiently long mixing times for the reagents and homogeneous Ag-shell growth. To limit the variation in particle volume when changing the Au-to-Ag ratios of the particles, both the core and the shell size of the Au core and Ag shell were varied. In this way, 3 batches of mesoporous silica coated Au-core Ag-shell NRs with an average atomic Ag fraction X_{Ag} of 0.20, 0.46, and 0.70 and an average particle volume V of 2.2, 4.1, and 5.6 × 10^4 nm^3, respectively, were obtained. To also investigate the influence of the particle volume on the atomic redistribution, a batch of considerably smaller Au@Ag@SiO_2 NRs with an average of X_{Ag} = 0.46 and V = 0.7 × 10^4 nm^3 was prepared.

In Table 1, we report a summary of the sample details, and in Figure 1, we show the corresponding high annular dark-field scanning transmission electron microscopy (HAADF-STEM) images and energy dispersive X-ray spectroscopy (EDX) maps. Due to the large Z contrast difference between Au and Ag atoms, the core−shell structure of the nanorods is readily visible in the HAADF-STEM images. The different Ag contents are most clearly seen in the EDX maps, in which Au and Ag are depicted in red and green, respectively. The Si signal of the silica shell is shown in Figure S1 together with the optical spectra (Figure S2) and a high-resolution TEM image showing the single crystalline structure of the nanorods (Figure S3).

Table 1. Sample Details for the Au@Ag@SiO_2 NRs Depicted in Figure 1[a]

X_{Ag}	L (nm)	D (nm)	$V \cdot 10^4$ (nm^3)
0.20	67 ± 10	21 ± 2.1	2.2 ± 0.58
0.46	74 ± 8.7	28 ± 1.9	4.1 ± 0.77
0.70	80 ± 9.2	32 ± 3.8	5.6 ± 1.6
0.46	48 ± 9.2	14 ± 1.8	0.7 ± 0.3

[a]The average and corresponding standard deviations of the atomic Ag fraction, length, diameter, and volume are indicated with X_{Ag}, L, D, and V, respectively. The values were based on 50 measurements per sample.

Direct Visualization of Metal Redistribution in Individual Particles with *in Situ* TEM. *In situ* TEM was used to visualize the atomic redistribution in individual NRs with different Au-to-Ag ratios and volumes. To avoid variations between *in situ* TEM measurements on different samples due to, *e.g.*, inequalities in the heating temperature or differences in electron dose that are known to be important in *in situ* electron microscopy,[28−30] we chose to compare four different samples in one measurement under exactly the same conditions. To achieve this, a mixture of the four samples with different Au-to-Ag ratios and particle volumes was deposited on a single SiN_x chip. The heating experiment was carried out in a high vacuum with a ramp of 3 °C/min. EDX analysis was used to map the Au and Ag metal distribution as a function of temperature.

Figure 2a shows the EDX maps of the mixture of Au@Ag@SiO_2 NRs at various temperatures. The EDX maps of the

DOI: 10.1021/acsnano.8b03978
ACS Nano 2018, 12, 8467−8476

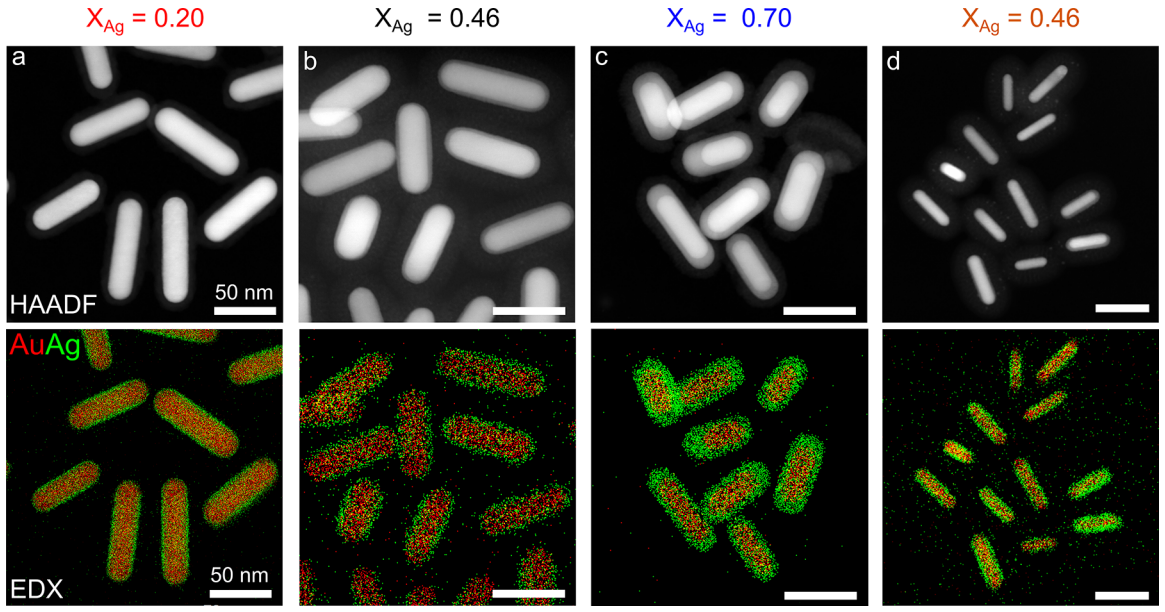

Figure 1. Electron microscopy images of mesoporous silica coated Au-core Ag-shell nanorods (Au@Ag@SiO_2 NRs) with different X_{Ag} ratios and particle volumes. Top: HAADF-STEM images. Bottom: EDX maps with Au and Ag in red and green, respectively. (a, red) Au@Ag@SiO_2 NRs with X_{Ag} = 0.20, V = 2.2 × 10^4 nm^3; (b, black) X_{Ag} = 0.46, V = 4.1 × 10^4 nm^3; (c, blue) X_{Ag} = 0.70, V = 5.6 × 10^4 nm^3; and (d, orange) X_{Ag} = 0.46, V = 0.7 × 10^4 nm^3. The Si signal is not shown in the EDX maps (see Figure S1).

orange, red, gray, and blue highlighted NRs in Figure 2a are enlarged in Figure 2b. We determined the Ag fractions and particle volumes of these individual nanorods, which were slightly different from the average values in Table 1: X_{Ag} = 0.44 V = 0.45 × 10^4 nm^3 (orange), X_{Ag} = 0.45 V = 5.0 × 10^4 nm^3 (black), X_{Ag} = 0.24 V = 3.0 × 10^4 nm^3 (red), and X_{Ag} = 0.68 V = 2.7 × 10^4 nm^3 (blue). To precisely track the metal redistribution in these individual nanorods during the heating process, we determined the core-to-shell ratio from the core and shell diameter for each particle at each temperature (see Figure S4 for details on the analysis procedure). From the core-to-shell ratios we derived the degree of alloying at the different heating temperatures, which increases from 0 to 1 when going from a core−shell to an alloyed nanorod. In Figure 2c, we plot the alloying curves of the black and orange highlighted single particles as a function of temperature for the 2 particles with the same Au−Ag ratio but have a differing particle volume by a factor of 10. The plot in Figure 2d shows the individual alloying curves of the particles in red, black, and blue, which have a similar volume but different Au-to-Ag ratios. We defined the alloying temperature T_{alloy} as the temperature at which the degree of alloying reached 0.5, which was 392, 394, 436, and 451 °C for the rods with X_{Ag} = 0.24, 0.44, 0.45, and 0.68, respectively.

These *in situ* TEM measurements clearly show the impact of the particle volume and the metal composition on the atomic redistribution, where a decrease in particle volume and Ag content led to significantly lower alloying temperatures. Lowering of the particle volume by a factor 10 (from V = 5.0 × 10^4 nm^3 to 0.45 × 10^4 nm^3) resulted in a decrease in alloying temperature of 42 °C, whereas the influence of the particle volume for larger NRs with V = 1.3 to 3.0 × 10^4 nm^3 was negligible (Figure S5). The considerable drop in the alloying temperature when decreasing the particle volume to V = 0.45 × 10^4 nm^3, and the diameter of the nanorod below 20 nm indicates an increased atom mobility at smaller particle dimensions. Such a size effect is in line with the previously reported particle-size-dependent melting of silica encapsulated AuNPs, in which the melting point decreased drastically from ∼900 to 300 °C when decreasing the (spherical) particle diameter from 20 to 1.5 nm.[34]

From EDX maps and corresponding alloying curves in Figure 2b,d, it is clear that the atomic redistribution is also strongly influenced by the Au−Ag ratio: the Au@Ag@SiO_2 NR with the X_{Ag} = 0.68 alloyed at almost 50 °C higher than the one with X_{Ag} = 0.24. Despite the fact that the rod with X_{Ag} = 0.68 had a volume 2 times smaller than that of the rod with X_{Ag} = 0.45, the increase in Ag content led to a significantly higher alloying temperature.

Ensemble-Averaged Atomic Redistribution from *in Situ* EXAFS. To investigate the impact of the metal composition on the atomic redistribution for a larger number of particles, we moved from *in situ* TEM to *in situ* EXAFS and extended our study from a femtogram to a milligram scale and from a single particle to 10^{19} particles. Additionally, *in situ* EXAFS measurements allowed the dosing of gases combined with a reliable temperature control. The unconventionally fast switching between the metal absorption edges (<1 min) at the ROCK beamline of the SOLEIL synchrotron made it possible to follow the atomic redistribution at the Au and Ag absorption edges in the same experiment. The alloying experiments were carried out under inert conditions in a He flow because the presence of oxygen is known to significantly change the alloying process.[8]

The *in situ* EXAFS data of the atomic redistribution in the Au@Ag@SiO_2 NRs with the lowest and highest Ag content, X_{Ag} = 0.20 and 0.70, are shown in Figure 3. Figure 3a−d shows the normalized $\mu(E)$ spectra and $\chi(k)$ spectra acquired at the Au L_3 and Ag K absorption edges of the NRs with X_{Ag} = 0.70. The oxidation state of the Au and Ag atoms in the core and in the shell of the NRs before heating was determined from the XAFS spectra at room temperature (RT) and found to be predominately metallic (Figure S6). The *in situ* EXAFS spectra show a clear change when heating the NRs from 30 to 500 °C.

DOI: 10.1021/acsnano.8b03978
ACS Nano 2018, 12, 8467−8476

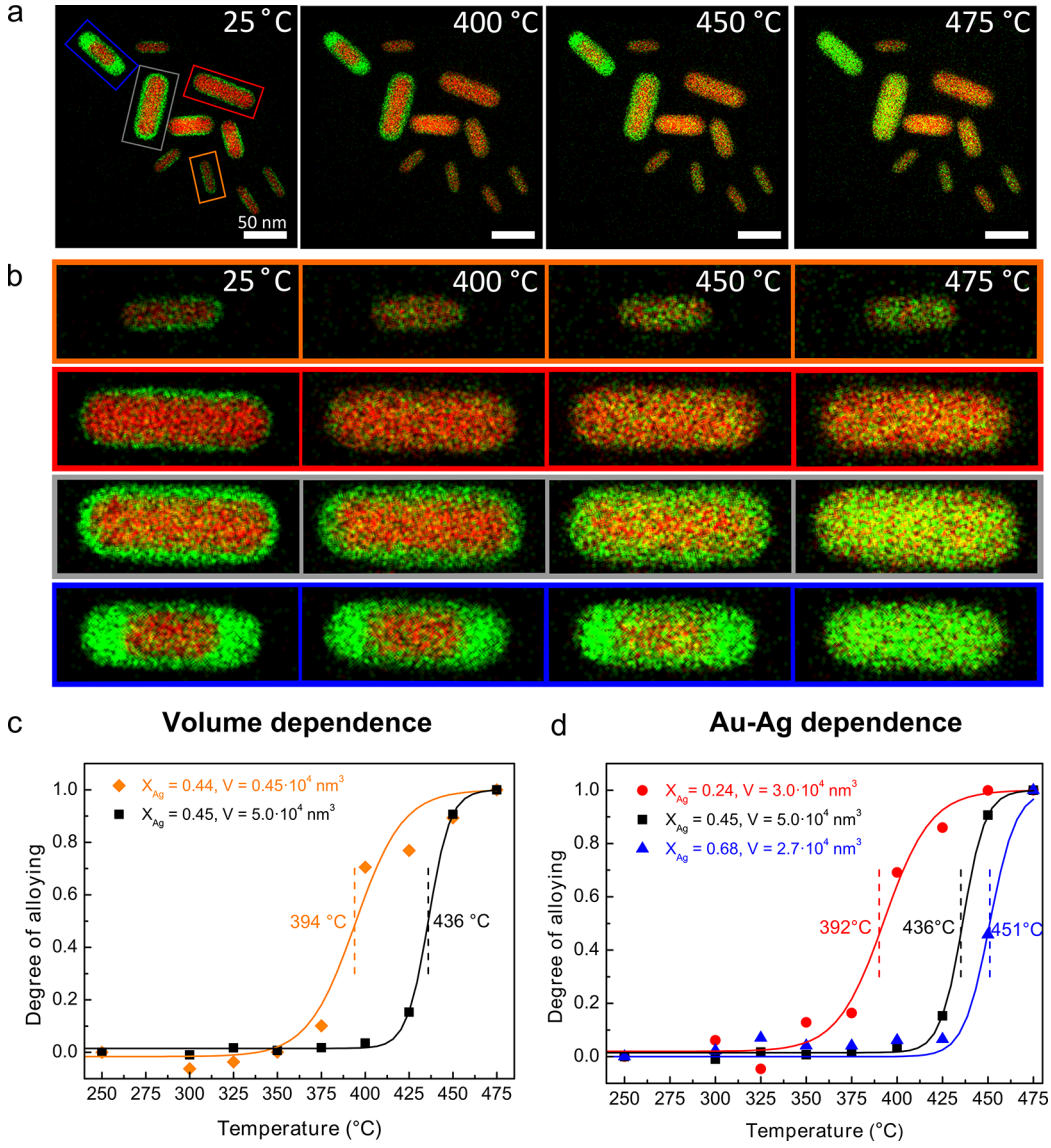

Figure 2. Direct visualization of atomic redistribution in individual Au@Ag@SiO_2 NRs with *in situ* heating TEM. (a, b) EDX maps acquired at 25, 400, 450, and 475 °C. (c) Particle volume dependence of the degree of alloying for Au@Ag@SiO_2 NRs with $V = 0.45 \times 10^4$ nm^3 (X_{Ag} = 0.44, orange) and $V = 5.0 \times 10^4$ nm^3 (X_{Ag} = 0.45, black). (d) The degree of alloying as a function of Ag-content with Au@Ag@SiO_2 NRs of X_{Ag} = 0.24 ($V = 3.0 \times 10^4$ nm^3, red), X_{Ag} = 0.45 ($V = 5.0 \times 10^4$ nm^3, black), and X_{Ag} = 0.68 ($V = 2.7 \times 10^4$ nm^3, blue). Curves are best fit to the experimental data. The heating ramp was set to 3 °C/min.

To verify if metal redistribution took place, we used the EXAFS spectra before and after thermal treatment to calculate the coordination numbers between the Au and Ag atoms: N_{Au-Au}, N_{Au-Ag}, N_{Ag-Ag}, and N_{Ag-Au}. Table 2 lists the coordination numbers for both samples. Due to the core−shell structure of the NRs, the coordination numbers between unlike atoms are low before heating. As expected, N_{Ag-Au} is lowest for core−shell particles with the highest X_{Ag}. After heating of the core−shell NRs to 500 °C, N_{Ag-Au} and N_{Au-Ag} increased by a factor of ≥6, indicating that mixing of the two elements took place in both samples. A full overview of the EXAFS fitting parameters is given in Tables S1−S4.

To estimate if the NRs were fully alloyed, meaning that the Au and Ag atoms were randomly dispersed within the particles, the extent of alloying (J) was calculated following the approach developed by Hwang et al.:[14]

$$J_{Au} = \frac{P_{observed}}{P_{random}} = \frac{[N_{Au-Ag}/(N_{Au-Ag} + N_{Au-Au})]_{observed}}{[N_{Au-Ag}/(N_{Au-Ag} + N_{Au-Au})]_{random}} \times 100\% \quad (1)$$

The J values of the two components (Au and Ag) give information on the internal distribution of the two components.[14] To calculate P_{random}, the Au-to-Ag ratios as determined by EDX were used. In Table 2, the J values for the two different NR samples before and after heating to 500 °C are given. For both alloyed samples, the calculated J_{Au} and J_{Ag} values are close to 100, indicating that the NRs are likely to have a fully alloyed structure when heating them to 500 °C.

To deduce the evolution of the alloying process from all the spectra acquired between 30 and 500 °C, we performed linear combination fitting on the normalized $\mu(E)$ spectra. In (E)XAFS analysis, linear combination fitting is typically used to determine and follow changes in the oxidation state of metal nanoparticles but is not common for following metal

DOI: 10.1021/acsnano.8b03978
ACS Nano 2018, 12, 8467−8476

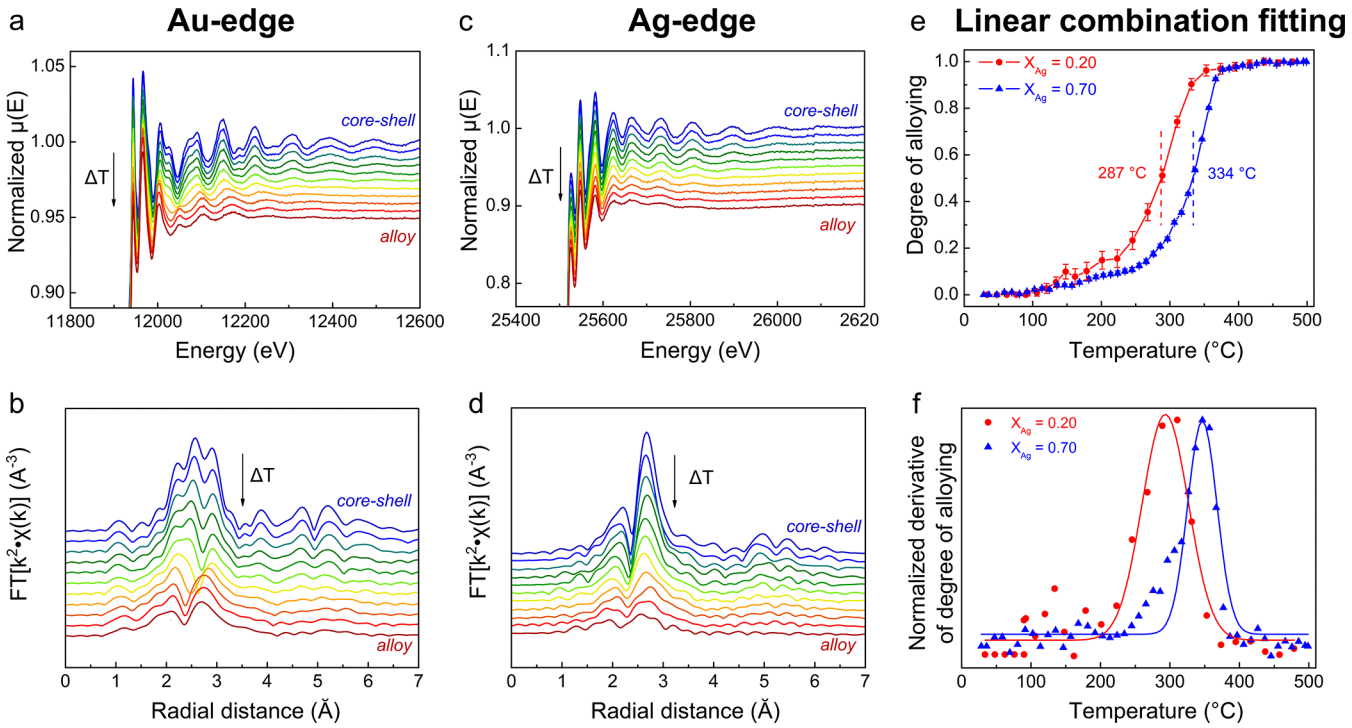

Figure 3. Double-edged *in situ* EXAFS measurements of Au@Ag@SiO_2 NRs upon heating. Normalized $\mu(E)$ spectra and FT$[k^2\chi(k)]$ spectra at the Au L_3 edge (panels a and b, Δk = 3.3−14.0 Å^{-1}) and Ag K edge (panels c and d, Δk = 3.2−12.0 Å^{-1}) of the nanorods with X_{Ag} = 0.70, recorded every ∼50 °C when heating from 30 to 500 °C. The plots in panels e and f show the degree of alloying and the derivative thereof as a function of temperature and were obtained by performing linear combination fitting on the normalized $\mu(E)$ spectra at the Ag K edge (X_{Ag} = 0.20, red) and Au L_3 edge (X_{Ag} = 0.70, blue). The EXAFS spectra were acquired during heating to 500 °C with 3 °C/min in a 25 mL/min He flow.

Table 2. Coordination Number *N* Before and After Heating the NRs to 500 °C in a 25 mL/min He Flow with a 3 °C/min Ramp[a]

	N_{Ag-Ag}	N_{Ag-Au}	N_{Au-Au}	N_{Au-Ag}	J_{Ag}	J_{Au}
X_{Ag} = 0.20 before heating	10.1 ± 1.8	1.1 ± 1.3	11.0 ± 0.2	0.3 ± 0.2	12	13
X_{Ag} = 0.20 after heating	2.5 ± 0.7	6.8 ± 1.7	9.6 ± 0.2	1.8 ± 0.1	91	79
X_{Ag} = 0.70 before heating	11.0 ± 0.3	0.6 ± 0.3	9.8 ± 0.2	0.3 ± 0.2	17	4
X_{Ag} = 0.70 after heating	7.7 ± 0.4	3.5 ± 0.2	3.1 ± 0.3	8.3 ± 0.4	104	104

[a]Based on the coordination numbers, the corresponding *J* values were calculated.

redistribution. Note that a linear combination fitting based analysis is considerably faster than calculation of the coordination numbers, which is especially important when analyzing a large number of EXAFS spectra.

In our analysis, each EXAFS spectrum at a given temperature was compared to the spectrum of the initial core−shell and final alloyed state for which the spectra at 30 and 500 °C were taken, respectively. As shown in Figure 3e, the analysis was successfully applied to obtain the degree of alloying as a function of temperature. Figure 3e specifically shows the linear combination fitting results determined from the Ag K edge for the X_{Ag} = 0.20 sample and the Au L_3 edge for the X_{Ag} = 0.70 sample because the change from core−shell to alloyed state is most apparent on the edge of the least abundant metal. In addition, it is important to note that the linear combination fitting analysis is also sensitive to changes that are not due to metal redistribution, such as the damping of the EXAFS spectra due to thermal disorder with increasing temperature. This temperature contribution predominately plays a role when the change upon alloying is small, as is the case for the absorption edge of the metal that is in the majority (Figures S7 and S8).

From Figure 3e, the alloying temperature determined at a degree of alloying of 0.5, was 287 and 334 °C for the sample with X_{Ag} = 0.20 and 0.70, respectively. The EXAFS measurements thus confirmed the increase in alloying temperature with increasing Ag content, as observed in the *in situ* TEM but now for a large ensemble of particles. However, it should be noted that there is a discrepancy in alloying temperatures: from the *in situ* EXAFS, we obtained ∼100 °C lower alloying temperatures compared with the *in situ* TEM data. This discrepancy demonstrates the need for *ex situ* measurements to establish the absolute temperature at which the metal redistribution occurs in the absence of an electron or X-ray beam.

Validation of the *in Situ* Data. Although electron microscopy and X-ray absorption spectroscopy enable the *in situ* observation of structural changes in metal nanoparticles, it is crucial to validate these techniques with *ex situ* measurements. In particular, electron beam irradiation has been reported to induce anomalous behavior in nanostructured

DOI: 10.1021/acsnano.8b03978
ACS Nano 2018, 12, 8467−8476

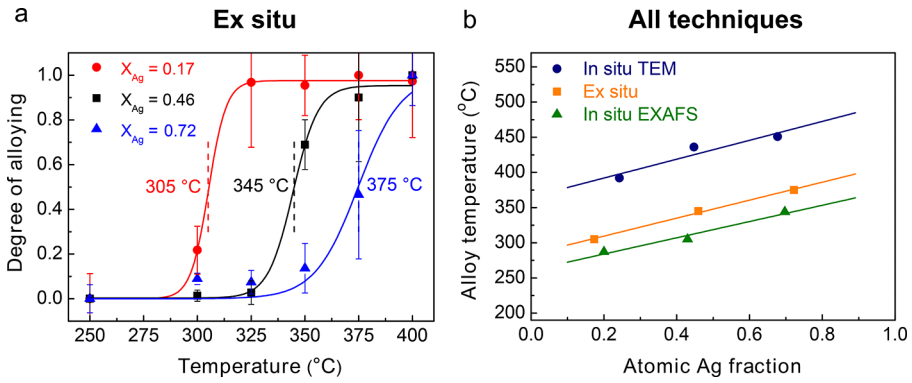

Figure 4. ***Ex situ*** **TEM measurements on the alloying of Au@Ag@SiO_2 NRs. (a) The degree of alloying after heating Au@Ag@SiO_2 NRs in a furnace as a function of the heating temperature. Each point is an average of four particles. The alloying temperatures for the Au@Ag@SiO_2 NRs with X_{Ag} = 0.17 (red), 0.46 (black), and 0.72 (blue) was 305, 345, and 375 °C, respectively. The samples were heated in a N_2 flow with a heating ramp of 3 °C/min. (b) A summary of the alloying temperature as a function of Ag fraction determined with** ***in situ*** **TEM (dark blue),** ***ex situ*** **TEM (orange), and** ***in situ*** **EXAFS (green). Curves are best fit to the experimental data.**

materials and significantly alter the deformation behavior, growth kinetics, and the structure of the nanoparticles during *in situ* studies.[28−30] To verify the dependence of the alloying temperature on the Au-to-Ag ratio, as observed in *in situ* TEM and *in situ* EXAFS, *ex situ* measurements were carried out by heating the NRs in a furnace. Herein, we used the same heating ramp of 3 °C/min to heat to 250, 300, 325, 350, 375, and 400 °C in N_2, after which each sample was analyzed with HAADF-STEM and EDX (Figure S9). In every sample and for each temperature, four representative rods were analyzed with EDX to determine their core-to-shell ratios and their compositions, which were close to the average sample compositions, as given in Table 1. From the core-to-shell ratio, the degree of alloying was calculated in the same way as described for the *in situ* TEM measurements, and the degree of alloying is shown as a function of the heating temperature in Figure 4a. It shows that the Au@Ag@SiO_2 NRs with average X_{Ag} values of 0.17, 0.46, and 0.72 alloy at 305, 345, and 375 °C, respectively. The EDX maps in Figure S9 show that all Au@Ag@SiO_2 NRs of the same composition simultaneously convert from a core−shell to the alloyed state.

In Figure 4b, an overview of the alloying temperatures versus the Ag content for all three techniques is shown. The *ex situ* data nicely support the trends observed in the *in situ* TEM and *in situ* EXAFS measurements. In all three techniques, the alloying temperature increases with increasing Ag content, and only the absolute temperatures vary. The *ex situ* TEM measurements match the EXAFS results, but the alloying temperatures determined by *in situ* TEM are 75−90 °C too high. The relatively high alloying temperatures from the *in situ* TEM measurements could be related to an altered heat conductivity in the SiN_X chip after depositing the nanorods combined with possible carbon contamination, leading to inaccurate temperatures in the heating chip. Alternatively, the strongly reducing electron beam could have influenced the kinetics of the alloying process, but we did not observe significant differences in the alloying process between areas that were or were not illuminated with the electron beam prior to the heating. Thus, although care should be taken in deducing quantitative data from *in situ* TEM, it is a powerful technique in providing a qualitative insight in the metal redistribution for single nanoparticles and correctly shows the dependency of the metal redistribution on the metal composition for different nanoparticles.

For all Au−Ag compositions, the observed alloying temperatures are far below the bulk melting point of Au and Ag, which points at a nanosize effect on the alloying process and enhanced atom mobilities compared to the bulk. Size effects have been observed for the melting temperatures of nanoparticles, where the melting point was significantly lowered when decreasing the nanostructure size.[34−36] Analogously, the observed lowering of the alloying temperature can be explained by a lowering in cohesive energy, which is the binding strength of the atom with its neighbors, with increasing particle surface to volume ratio.[37,38] Because the cohesive energy is proportional to the vacancy formation energy and activation energy of diffusion, it is to be expected that the mobility of atoms and the rate of alloying increases for smaller nanostructures, leading to lower alloying temperatures. When decreasing the particle diameter below 5 nm, even spontaneous alloying of bimetallic Au−Ag nanoparticles at room temperature can occur.[39]

It should be noted that the observed trend between the alloying temperature and metal composition in the Au−Ag nanoparticles varies oppositely to the composition dependency in the melting point temperature, where $T_{melting,Ag}$ = 962 and $T_{melting,Au}$ = 1064 °C. A similar trend for atomic diffusion was measured in bulk Au−Ag crystals.[40] The activation energy of diffusion for both Au and Ag atoms in Au−Ag alloys was reported to increase with increasing Ag fraction going from 1.74 to 1.93 eV for Ag atoms in pure Au and Ag and 1.81 to 2.09 eV for Au atoms in pure Au and Ag.[40] From these activation energies, it follows that Ag atoms are more mobile than Au atoms but that the diffusion of both Au and Ag atoms is slower in high-Ag-content Au−Ag alloys. A possible explanation for this phenomenon can be derived from the energy of vacancy formation and atom migration, which are known to be higher in Ag compared to Au: E(vacancy formation)$_{Ag}$ = 1.10 eV, E(vacancy formation)$_{Au}$= 0.97 eV, E(atom migration)$_{Ag(in)Ag}$ = 0.83 eV, and E(atom migration)$_{Ag(in)Au}$ = 0.77 eV.[40−42] Because atomic diffusion in Au−Ag crystals is known to go via vacancy-hopping, a lower number of vacancies and a higher energy cost for hopping into the vacancies with increasing Ag content could explain the observed retardation of Au and Ag in high-content Ag alloys. In addition to Au−Ag, similar trends of self-diffusion dependency opposite to melting temperature have been reported for, *e.g.*, Ag−Mn,[43] Ti−Cr,[44,45] and Tl−Pb bulk

DOI: 10.1021/acsnano.8b03978
ACS Nano 2018, 12, 8467−8476

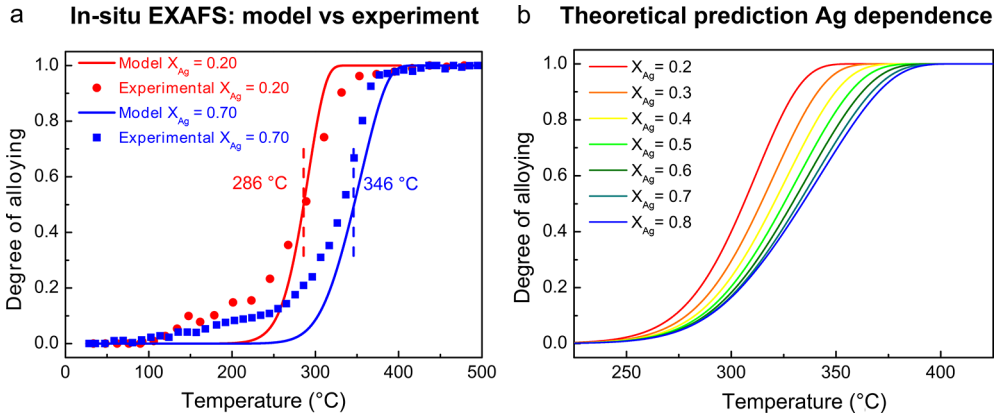

Figure 5. Theoretical prediction of the change in the degree of alloying as a function of heating temperature and atomic Ag fraction. (a) The theoretical prediction for the *in situ* EXAFS experiment give an alloying temperature of 286 and 346 °C for the samples with X_{Ag} = 0.20 and 0.70. The plot in panel b shows the theoretical prediction of the alloying curves for Au−Ag NRs of $V = 4 \times 10^4$ nm^3 and X_{Ag} = 0.2−0.8 (from red to blue) heated with 3 °C/min.

crystals.[46] In this study, we show experimental proof of this trend at the nanoscale.

Modeling Atomic Redistribution. We devised a simple model that can correctly describe the diffusion in Au−Ag nanoparticles as a function of temperature and composition. We numerically calculate the diffusion of Au atoms n_{Au} and Ag atoms n_{Ag} passing through a static Au−Ag interface per time step Δt according to Fick's first law:

$$n_{Ag}/\Delta t = (A/r) \times D_0^{Ag} e^{-Q_{Ag}/(RT)} \times |C_{core}^{Ag} - C_{shell}^{Ag}| \quad (2)$$

where A is the interface area, r the radius of the NP, D_0^{Ag} the frequency factor, Q_{Ag} the activation energy, R the gas constant, T the temperature, C_{core}^{Ag} the silver concentration of the core, and C_{shell}^{Ag} the silver concentration of the shell (expressed in atoms per cubic meter). An analogous formula holds for the Au atoms. The rate of diffusion was calculated iteratively, where D_0, Q, and the concentration difference $C_{core} - C_{shell}$ were updated every time step. The frequency factor D_0 and activation energy for diffusion Q depend on the Au−Ag composition and have been measured experimentally in bulk crystals.[40] We corrected these composition-dependent bulk D_0 and Q values for the NP size according to the model of Guisbiers et al.[47,48] Herein, the activation energy of diffusion in NPs Q_{NP} was derived from the activation energy of diffusion in the bulk Q_{bulk} by using a so-called shape factor α_{shape}, which, among others, depends on the surface-to-volume ratio of the NPs. More details on the calculation of the α_{shape} factor can be found in the Experimental section. For the Au−Ag NRs used in this study, the correction of Q_{bulk} to Q_{NP}, resulted in alloy temperatures of ∼50 °C lower compared with bulk crystals of the same Au−Ag composition.

The resulting theoretical predictions for the alloying curves of the *in situ* EXAFS measurements are shown in Figure 5a. The theoretical predictions are in very good agreement with the experimental *in situ* EXAFS data, and the alloying temperatures as predicted by the model, 286 and 346 °C for the X_{Ag} = 0.20 and 0.70, respectively, match the experimental values of 287 and 334 °C closely. In Figure 5b, we show the theoretical prediction for the alloying curves of Au−Ag NRs with $V = 4 \times 10^4$ nm^3 and X_{Ag} = 0.2−0.8. In the calculation of these curves a heating ramp of 3 °C/min was considered, as in the experimental studies. The theoretical predictions clearly demonstrate the importance of including the dependency of the diffusion on the metal composition. We stress that it is remarkable that the metal composition still plays such a crucial role in the diffusion kinetics in nanoparticles, in which size and shape have generally been considered to play the most-important role,[12,33,47] and the influence of the particle composition has therefore been neglected so far.

CONCLUSIONS

We have used a multitechnique approach to precisely follow metal redistribution, a process crucial in catalysis, *in situ*, and at different length scales. A combination of *in situ* TEM with *in situ* EXAFS validated with *ex situ* measurements provided both a single particle and ensemble-averaged characterization. Our well-defined model system, consisting of mesoporous silica-coated, single-crystalline Au-core Ag-shell nanorods of tunable size and composition, allowed a systematic study of the nanoparticle composition on the atomic redistribution kinetics. We unambiguously showed that the atomic diffusion in Au−Ag nanoparticles strongly depends on the composition, a trend that has been observed in bulk crystals but that has, to the best of our knowledge, not been reported for nanomaterials. Additionally, we find indications for a nanoscale effect on the alloying process, leading to lower alloying temperatures when decreasing the nanoparticle size. Finally, we show that to correctly model metal redistribution in metallic nanoparticles, not only the nanoscale dimensions but also the metal composition should be taken into account. Both our experimental approach and the theoretical model are likely to apply to a wide range of bimetallic nanoparticle-based materials.

EXPERIMENTAL SECTION

Chemicals. All chemicals were used as received without further purification. Hexadecyltrimethylammonium bromide (CTAB, >98.0%) and sodium oleate (NaOL, >97.0%) were purchased from TCI America. Hydrogen tetrachloroaurate trihydrate ($HAuCl_4 \cdot 3H_2O$) and sodium hydroxide (98%) were purchased from Acros Organics. L-Ascorbic Acid (BioXtra, ≥ 99%), silver nitrate ($AgNO_3$, ≥ 99%), sodium borohydride ($NaBH_4$, 99%), hydrochloric acid (HCl, 37 wt % in water), tetraethyl orthosilicate (TEOS, 98%), and ammonium hydroxide solution (≥25 wt % in water) were purchased from Sigma-Aldrich. Ultrapure water (Millipore Milli-Q grade) with a resistivity of 18.2 MΩ was used in all of the experiments. All glassware for the AuNR synthesis was cleaned with fresh aqua regia (HCl/

DOI: 10.1021/acsnano.8b03978
ACS Nano 2018, 12, 8467−8476

HNO_3 in a 3:1 volume ratio), rinsed with large amounts of water and dried at 100 °C before usage.

Synthesis of the Au−Ag Nanorods. A total of three batches of Au@Ag@SiO_2 NRs with average Ag atomic fractions of 0.20, 0.46, and 0.70 were prepared by changing both the Au-core size and the Ag-shell thickness. The synthesis of the AuAg core−shell rods consists of four steps: AuNR synthesis (1), mesoporous silica coating (2), partial etching of AuNRs within their mesoporous silica shells (3), and Ag-shell growth on the etched AuNRs (4).

In the first step, monodisperse AuNRs were synthesized according to the protocol of Ye et al.[49] A pair of 500 mL scale syntheses were carried out with growth solutions containing 7.0 g of CTAB, 1.24 g of NaOL, 25 mL of MQ H_2O, and 250 mL of 1.0 mM $HAuCl_4$; 7.2 mL of $AgNO_3$; 2.1 mL of concentrated HCl; 64 mM ascorbic acid; and 1.0 mL of seed solution. The seeds were prepared from 10 mL of 0.10 M CTAB, 51 μL of $HAuCl_4$ and 1.0 mL of $NaBH_4$. The subsequent rod growth was performed under static conditions in a 30 °C water bath overnight. The resulting AuNR suspensions had an absorption maximum of 4.0 at λ(LSPR) = 866 and 853 nm. The rods were centrifuged at 8000 rcf for 30 min (Rotina 380R Hettich centrifuge), washed with H_2O, and redispersed in 5.0 mM CTAB H_2O.

In the second step, the CTAB stabilized AuNRs were coated with a 18 nm mesoporous silica shell via the method of Gorelikov et al.[32] The coating was performed in 350 mL of 1.5 mM CTAB aqueous solution containing 1.0 mM NaOH and an AuNR concentration corresponding to a absorption maximum of 10. During magnetic stirring at 300 rpm in a 30 °C water bath, 3 times 1.05 mL of 20 vol % TEOS in EtOH were added with a 30 min time interval. The Au@SiO_2 NRs were centrifuged at 8000 rcf for 30 min and washed with water and ethanol.

The third step, oxidative etching of the Au@SiO_2 NRs, was performed by following the procedure described by Deng et al.[9] but with H_2O_2 as an oxidant instead of O_2 from air. Different core sizes were obtained by varying the etching time. For the rods with X_{Ag} = 0.20, 240 mL of AuNRs in MeOH (Abs = 6.0) were heated to 60 °C in an oil bath while magnetically stirring at 400 rpm with 4.8 mL of HCl (37%) and 4.8 mL of H_2O_2 (0.2 wt %). The LSPR peak position changed from 838 to 822 nm after etching for 10 min. The reaction was quenched by putting the mixture in a 4 °C water bath and diluting it with 200 mL of ice-cold MeOH before centrifugation at 10000 rcf for 20 min. The etched rods were washed with and redispersed in EtOH. For batches with X_{Ag} = 0.46 and 0.70, 210 mL of AuNRs in MeOH, 4.8 mL of HCl (37%), and 4.8 mL of H_2O_2 (0.2 wt %) were added. After 13 and 26 min, 100 mL of reaction mixture was quenched with 100 mL of ice-cold MeOH and was as described above. The LSPR peak positions of the rods were 750 and 694 nm.

Finally, the procedure by Deng et al. was modified to do the Ag overgrowth in large reaction volumes (≫ 1 mL). HCl was added to lower the Ag reduction rate by ascorbic acid and allows for a homogeneous shell growth on all particles. The rods with X_{Ag} = 0.20 were prepared by adding 2.0 mL of 0.1 M HCl, 3.0 mL of 5.0 mM $AgNO_3$, and 3.0 mL of 20 mM ascorbic acid were added to 200 mL of aqueous AuNR suspension (Abs = 4.5, LSPR = 780 nm) while stirring vigorously. The rods with X_{Ag} = 0.70 were prepared in 2 steps. To 120 mL of rod suspension was added 1.2 mL of 0.1 M HCl, 6.6 mL of 5.0 mM $AgNO_3$, and 6.6 mL of 20 mM ascorbic acid. After washing with MQ H_2O, a second Ag-overgrowth step was performed to increase the Ag content. To 100 mL of aqueous Au@Ag@SiO_2 NR suspension (Abs = 1.2, LSPR = 701 nm), 1.0 mL of 0.1 M HCl, 4.0 mL of 5.0 mM $AgNO_3$, and 4.0 mL of 20 mM ascorbic acid were added. The X_{Ag} = 0.46 sample was prepared on a smaller scale because it was only used for the *ex situ* and *in situ* TEM measurements. To 1.0 mL of aqueous Au@SiO_2 NRs suspension (Abs = 2.5, LSPR = 745 nm), 10 μL of 0.1 M HCl, 40 μL of 5.0 mM $AgNO_3$, and 40 μL of 20 mM ascorbic acid were added.

All Au@Ag@SiO_2 NRs were washed with MQ H_2O and ethanol, redispersed in ethanol, and stored at 4 °C to prevent oxidation and dissolution of the Ag shell. The centrifugation speed varied between 6000 and 8000 rcf depending on the volume of the rods. The samples were dried at 60 °C in air. All samples were characterized with visible−near-infrared spectroscopy and TEM.

***In Situ* TEM.** The *in situ* heating measurements were carried out on a FEI Talos F200X operated at 200 kV using a heating holder from DENSsolutions. A mix of four different batches of Au@Ag@SiO_2 NRs was drop-cast on a heating chip (Wildfire Nanochip) with silicon nitride windows. The overall heating ramp was set to 3 °C/min. EDX maps were acquired at 25, 250, 300, and 350 °C and from 400 to 650 °C with a 25 °C temperature interval. The acquisition time per EDX map was 5 min, and the probe current was 700 pA. In the intervals between the EDX acquisitions, the beam was blanked to minimize the influence of the electron beam on the alloying process. Different SiN windows were checked during heating that were not illuminated prior to heating. No significant differences in alloying kinetics were observed between the illuminated and non-illuminated spots. The SiN chip was plasma was cleaned for 10 s in a 20% O_2 in an Ar atmosphere before the TEM experiment.

***In Situ* EXAFS.** The *in situ* EXAFS measurements were performed at the ROCK beamline of the SOLEIL synchrotron. At this beamline, continuous switching between the Au L_3 edge (11919 eV) and the Ag K edge (25514 eV) is possible (time to switch ∼1 min) using two Quick-XAS monochromators equipped with Si(111) and Si(220) channel-cut crystals, respectively. The operation parameters of the monochromators were set to record two EXAFS spectra per second. The powdered samples were loaded in a stainless steel sample holder (with a depth of 1 mm) allowing temperature control and gas flow. The X_{Ag} = 0.20 and 0.70 Au@Ag@SiO_2 NR samples were diluted with boron nitride. The heating was done in a He flow of 25 mL/min and with a heating rate of 3 °C/min. Before and after heating, EXAFS spectra were collected for 500 s at each edge at room temperature and averaged. During the temperature ramps, alternate measurements at both edges were performed continuously: spectra were collected and averaged for 35 s at the Au edge and 60 to 120 s at the Ag edge, depending on the quality of the Ag signal. Measurements were done in transmission mode using ionization chambers as detectors. Energy calibration was ensured by the simultaneous measurement of the absorption spectra of metallic Au and Ag foils.

Spectra analysis was conducted with the IFEFFIT library using the GUI Athena and Artemis.[50] All spectra were energy calibrated to the first inflection point of the Ag or Au foil at 25 514 and 11 919 eV, respectively. EXAFS signal was extracted in Athena with a R = 1.0 cutoff and a k weight of 2 and Fourier transformed using a Hanning window in k = 3 and dk = 1. EXAFS analysis was conducted in Artemis with the normalized spectra exported from Athena. The amplitude reduction factor (S_0^2) of 0.83 for Ag and 0.79 for Au was obtained by fitting the EXAFS data of the respective metal foils. The simulation of scattering paths for the bi-metallic samples was performed with the ATOMS algorithm with a custom input file created by substituting Au atoms by Ag in the first shell to obtain the closest rational fraction of atoms. A correction factor was introduced to S_0^2 to obtain the actual sample composition. Structural parameters were determined by multiple k-weight least-squares fitting, and the goodness of fit was determined by observing the reduced χ^2 and R^2 statistical parameters. The linear combination fitting was carried out in Athena on the normalized $\mu(E)$ spectra in the region between −20 to 120 eV from the absorption edge.

***Ex situ* Heating.** The *ex situ* heating experiments were performed in a tubular oven (Thermolyne 79300 tube furnace) under a constant N_2 flow. The three different samples were each drop-cast on a copper TEM grid (200 mesh copper (100), Formvar/carbon film) and heated in a ceramic cup placed in a quartz oven tube. The heating rate was always 3 °C/min, and the particles were heated to 250, 300, 325, 350, 375, and 400 °C and cooled under N_2 to room temperature before taking them out of the oven. After heating, all samples were analyzed with HAADF and EDX on a FEI Talos F200X, operated under the same conditions as described above.

Diffusion Model. To predict the rate of alloying in Au−Ag nanoparticles, we numerically calculated Fick's first law. The number of Au, n_{Au}, and Ag atoms, n_{Ag}, diffusing through the static Au−Ag interface per time step was calculated with eq 2. After each step, the

DOI: 10.1021/acsnano.8b03978
ACS Nano 2018, 12, 8467−8476

Au-to-Ag ratio of the core and the shell was updated, affecting D_0, Q, C_{core}, and C_{shell} in eq 2. The values for D_0 and Q for silver and gold diffusing into various Au−Ag compositions were taken from the work of Mallard et al.[40] These bulk values of D_0 and Q were corrected for NP size effects according to the model of Guisbiers,[47,48] in which the change in activation energy for a NP compared to the activation energy in the bulk can be described as:

$$\frac{Q_{NP}}{Q_{bulk}} = 1 - \frac{\alpha_{shape}}{D} \quad (3)$$

where the shape factor α_{shape} is given by:[47]

$$\alpha_{shape} = \frac{D(\gamma_s - \gamma_l)}{\Delta H_{m,\infty}} \times \frac{S}{V} \quad (4)$$

Here, D is the diameter of the NP; $\gamma_{s,l}$ are the surface energies in the solid and the liquid phases, respectively; S the surface area of the NP; V the volume of the NP; and $\Delta H_{m,\infty}$ the bulk melting enthalpy.

Lastly, the temperature was updated every time step according to the temperature ramp used in the experiments. Usually, one time step was 1 s, which ensured small changes in the Au−Ag content per time step for the temperatures used in this work. Subsequent time steps were evaluated until the core and shell consist of the same Au−Ag composition, when a full alloy composition is reached. Only geometric input parameters determined from TEM such as the core−shell volume, the interface and surface area and the radius of the NP were needed for the calculations.

ASSOCIATED CONTENT

Supporting Information

The Supporting Information is available free of charge on the ACS Publications website at DOI: 10.1021/acsnano.8b03978.

Figures showing EDX maps, optical spectra of the different batches of Au@Ag@SiO_2 NRs, high-resolution TEM images, the analysis method that was used to deduce the degree of alloying from the EDX maps, additional alloying curves derived from the *in situ* TEM measurements, additional EXAFS spectra, and alloying curves. Tables showing the fitting parameters used to calculate the coordination numbers from the EXAFS data. (PDF)

AUTHOR INFORMATION

Corresponding Authors

*E-mail: A.vanBlaaderen@uu.nl.

*E-mail: P.E.deJongh@uu.nl.

ORCID

Petra E. de Jongh: 0000-0002-2216-2620

Notes

The authors declare no competing financial interest.

ACKNOWLEDGMENTS

The authors thank Dr. M.A. van Huis for providing the *in situ* electron microscopy heating equipment, M. Bransen for useful discussion on the nanorod synthesis, and Dr. S. Dussi for critically reading the manuscript. This project has received funding from the European Research Council (ERC) under the European Union's Horizon 2020 research and innovation programme (ERC-2014-CoG no. 648991) and the ERC under the European Unions Seventh Framework Programme (FP-2007-2013) and ERC Advanced Grant Agreement no. 291667 HierarSACol. J.v.d.H. also acknowledges the Graduate programme of the Debye Institute for Nanomaterials Science (Utrecht University), which is facilitated by the grant 022.004.016 of the NWO, The Netherlands Organisation for Scientific Research. The authors acknowledge the award of beamtime on the ROCK beamline at Synchrotron SOLEIL under proposal no. 20151175. The work on ROCK beamline was supported by a public grant overseen by the French National Research Agency (ANR) as a part of the "Investissements d'Avenir" program (ref no. ANR-10-EQPX-45).

REFERENCES

(1) Gilroy, K. D.; Ruditskiy, A.; Peng, H.-C.; Qin, D.; Xia, Y. Bimetallic Nanocrystals: Syntheses, Properties, and Applications. *Chem. Rev.* **2016**, *116*, 10414−10472.

(2) de Aberasturi, D. J.; Serrano-Montes, A. B.; Liz-Marzán, L. M. Modern Applications of Plasmonic Nanoparticles: From Energy to Health. *Adv. Opt. Mater.* **2015**, *3*, 602−617.

(3) Ferrando, R.; Jellinek, J.; Johnston, R. L. Nanoalloys: From Theory to Applications of Alloy Clusters and Nanoparticles. *Chem. Rev.* **2008**, *108*, 845−910.

(4) Singh, A. K.; Xu, Q. Synergistic Catalysis over Bimetallic Alloy Nanoparticles. *ChemCatChem* **2013**, *5*, 652−676.

(5) Liu, X.; Wang, A.; Yang, X.; Zhang, T.; Mou, C. Y.; Su, D. S.; Li, J. Synthesis of Thermally Stable and Highly Active Bimetallic Au-Ag Nanoparticles on Inert Supports. *Chem. Mater.* **2009**, *21*, 410−418.

(6) Sun, K. Q.; Hong, Y. C.; Zhang, G. R.; Xu, B. G. Synergy between Pt and Au in Pt-on-Au Nanostructures for Chemoselective Hydrogenation Catalysis. *ACS Catal* **2011**, *1* (10), 1336−1346.

(7) Hong, J. W.; Kim, D.; Lee, Y. W.; Kim, M.; Kang, S. W.; Han, S. W. Atomic-Distribution-Dependent Electrocatalytic Activity of Au-Pd Bimetallic Nanocrystals. *Angew. Chem., Int. Ed.* **2011**, *50*, 8876−8880.

(8) Albrecht, W.; Van Der Hoeven, J. E. S.; Deng, T. S.; De Jongh, P. E.; van Blaaderen, A. Fully Alloyed Metal Nanorods with Highly Tunable Properties. *Nanoscale* **2017**, *9*, 2845−2851.

(9) Deng, T. S.; Van Der Hoeven, J. E. S.; Yalcin, A. O.; Zandbergen, H. W.; Van Huis, M. A.; Van Blaaderen, A. Oxidative Etching and Metal Overgrowth of Gold Nanorods within Mesoporous Silica Shells. *Chem. Mater.* **2015**, *27*, 7196−7230.

(10) Gao, C.; Hu, Y.; Wang, M.; Chi, M.; Yin, Y. Fully Alloyed Ag/Au Nanospheres: Combining the Plasmonic Property of Ag with the Stability of Au. *J. Am. Chem. Soc.* **2014**, *136*, 7474−7479.

(11) Bonifacio, C. S.; Carenco, S.; Wu, C. H.; House, S. D.; Bluhm, H.; Yang, J. C. Thermal Stability of Core-Shell Nanoparticles: A Combined In Situ Study by XPS and TEM. *Chem. Mater.* **2015**, *27*, 6960−6968.

(12) Lasserus, M.; Schnedlitz, M.; Knez, D.; Messner, R.; Schiffmann, A.; Lackner, F.; Hauser, A. W.; Hofer, F.; Ernst, W. E. Thermally Induced Alloying Processes in a Bimetallic System at the Nanoscale: AgAu sub-5 nm Core-Shell Particles Studied at Atomic Resolution. *Nanoscale* **2018**, *10*, 2017−2024.

(13) Pramanik, S.; Chattopadhyay, S.; Das, J. K.; Manju, U.; De, G. Extremely Fast Au-Ag Alloy-Dealloy Associated Reversible Plasmonic Modifications in SiO_2 Films. *J. Mater. Chem. C* **2016**, *4*, 3571−3580.

(14) Hwang, B. J.; Sarma, L. S.; Chen, J. M.; Chen, C. H.; Shih, S. C.; Wang, G. R.; Liu, D. G.; Lee, J. F.; Tang, M. T. Structural Models and Atomic Distribution of Bimetallic Nanoparticles as Investigated by X-ray Absorption Spectroscopy. *J. Am. Chem. Soc.* **2005**, *127*, 11140−11145.

(15) Ding, Y.; Fan, F.; Tian, Z.; Wang, Z. Atomic Structure of Au-Pd Bimetallic Alloyed Nanoparticles. *J. Am. Chem. Soc.* **2010**, *132*, 12480−12486.

(16) Masoud, N.; Delannoy, L.; Calers, C.; Gallet, J. J.; Bournel, F.; de Jong, K. P.; Louis, C.; de Jongh, P. E. Silica-Supported Au-Ag Catalysts for the Selective Hydrogenation of Butadiene. *ChemCatChem* **2017**, *9*, 2418−2425.

(17) Zugic, B.; Wang, L.; Heine, C.; Zakharov, D. N.; Lechner, B. A. J.; Stach, E. A.; Biener, J.; Salmeron, M.; Madix, R. J.; Friend, C. M. Dynamic Restructuring Drives Catalytic Activity on Nanoporous Gold-Silver Alloy Catalysts. *Nat. Mater.* **2016**, *16*, 558−565.

DOI: 10.1021/acsnano.8b03978
ACS Nano 2018, 12, 8467−8476

(18) Destro, P.; Kokumai, T. M.; Scarpellini, A.; Pasquale, L.; Manna, L.; Colombo, M.; Zanchet, D. The Crucial Role of the Support in the Transformations of Bimetallic Nanoparticles and Catalytic Performance. *ACS Catal.* **2018**, *8*, 1031−1037.
(19) Sandoval, A.; Aguilar, A.; Louis, C.; Traverse, A.; Zanella, R. Bimetallic Au-Ag/TiO_2 Catalyst Prepared by Deposition- Precipitation: High Activity and Stability in CO Oxidation. *J. Catal.* **2011**, *281*, 40−49.
(20) Tao, F.; Salmeron, M. In Situ Studies of Chemistry and Structure of Materials in Reactive Environments. *Science* **2011**, *331*, 171−174.
(21) Xin, H. L.; Alayoglu, S.; Tao, R.; Genc, A.; Wang, C. M.; Kovarik, L.; Stach, E. A.; Wang, L. W.; Salmeron, M.; Somorjai, G. A.; Zheng, H. Revealing the Atomic Restructuring of Pt-Co Nanoparticles. *Nano Lett.* **2014**, *14*, 3203−3207.
(22) Holse, C.; Elkjær, C. F.; Nierhoff, A.; Sehested, J.; Chorkendorff, I.; Helveg, S.; Nielsen, J. H. Dynamic Behavior of CuZn Nanoparticles Under Oxidizing and Reducing Conditions. *J. Phys. Chem. C* **2015**, *119*, 2804−2812.
(23) Tao, F.; Grass, M. E.; Zhang, Y.; Butcher, D. R.; Renzas, J. R.; Liu, Z.; Chung, J. Y.; Mun, B. S.; Salmeron, M.; Somorjai, G. A. Reaction-Driven Restructuring of Rh-Pd and Pt-Pd Core-Shell Nanoparticles. *Science* **2008**, *322*, 932−934.
(24) Ahmadi, M.; Behafarid, F.; Cui, C.; Strasser, P.; Cuenya, B. R. Long-Range Segregation Phenomena in Shape-Selected Bimetallic Nanoparticles: Chemical State Effects. *ACS Nano* **2013**, *7*, 9195−9204.
(25) Carenco, S.; Wu, C. H.; Shavorskiy, A.; Alayoglu, S.; Somorjai, G. A.; Bluhm, H.; Salmeron, M. Synthesis and Structural Evolution of Nickel-Cobalt Nanoparticles Under H_2 and CO_2. *Small* **2015**, *11*, 3045−3053.
(26) Hodak, J. H.; Henglein, A.; Giersig, M.; Hartland, G. V. Laser-Induced Inter-Diffusion in AuAg Core-Shell Nanoparticles. *J. Phys. Chem. B* **2000**, *104*, 11708−11718.
(27) Liao, H.; Fisher, A.; Xu, Z. J. Surface Segregation in Bimetallic Nanoparticles: A Critical Issue in Electrocatalyst Engineering. *Small* **2015**, *11*, 3221−3246.
(28) Sarkar, R.; Rentenberger, C.; Rajagopalan, J. Electron Beam Induced Artifacts During In Situ TEM Deformation of Nanostructured Metals. *Sci. Rep.* **2015**, *5*, 1−11.
(29) Woehl, T. J.; Evans, J. E.; Arslan, I.; Ristenpart, W. D.; Browning, N. D. Direct In Situ Determination of the Mechanisms Controlling Nanoparticle Nucleation and Growth. *ACS Nano* **2012**, *6*, 8599−8610.
(30) Van Den Berg, R.; Elkjaer, C. F.; Gommes, C. J.; Chorkendorff, I.; Sehested, J.; De Jongh, P. E.; De Jong, K. P.; Helveg, S. Revealing the Formation of Copper Nanoparticles from a Homogeneous Solid Precursor by Electron Microscopy. *J. Am. Chem. Soc.* **2016**, *138*, 3433−3442.
(31) Frenkel, A. I. Applications of Extended X-ray Absorption Fine-Structure Spectroscopy to Studies of Bimetallic Nanoparticle Catalysts. *Chem. Soc. Rev.* **2012**, *41*, 8163−8178.
(32) Gorelikov, I.; Matsuura, N. Supporting Information Single-Step Coating of Mesoporous Silica on CTAB- Capped Nanoparticles. *Nano Lett.* **2008**, *8*, 369−373.
(33) Guisbiers, G.; Mendoza-Cruz, R.; Bazán-Dıaz, L.; Velázquez-Salazar, J. J.; Mendoza-Perez, R.; Robledo-Torres, J. A.; Rodriguez-Lopez, J. L.; Montejano-Carrizales, J. M.; Whetten, R. L.; José-Yacamán, M. Electrum, the Gold-Silver Alloy, From the Bulk Scale to the Nanoscale: Synthesis, Properties, and Segregation Rules. *ACS Nano* **2016**, *10*, 188−198.
(34) Dick, K.; Dhanasekaran, T.; Zhang, Z.; Meisel, D. Size-Dependent Melting of Silica-Encapsulated Gold Nanoparticles. *J. Am. Chem. Soc.* **2002**, *124*, 2312−2317.
(35) Buffat, P.; Borel, J.-P. Size Effect on the Melting Temperature of Gold Partlcles. *Phys. Rev. A: At., Mol., Opt. Phys.* **1976**, *13*, 2287−2298.
(36) Castro, T.; Reifenberger, R.; Choi, E.; Andres, R. P. Size-Dependent Melting Temperature of Individual Nanometer-Sized Metallic Clusters. *Phys. Rev. B: Condens. Matter Mater. Phys.* **1990**, *42*, 8548−8556.
(37) Yang, C. C.; Li, S. Investigation of Cohesive Energy Effects on Size-Dependent Physical and Chemical Properties of Nanocrystals. *Phys. Rev. B: Condens. Matter Mater. Phys.* **2007**, *75*, 165413.
(38) Nanda, K. K.; Sahu, S. N.; Behera, S. N. Liquid-Drop Model for the Size-Dependent Melting of Low-Dimensional Systems. *Phys. Rev. A: At., Mol., Opt. Phys.* **2002**, *66*, 013208.
(39) Shibata, T.; Bunker, B. A.; Zhang, Z.; Meisel, D.; Vardeman, C. F.; Gezelter, J. D. Size-Dependent Spontaneous Alloying of Au-Ag Nanoparticles. *J. Am. Chem. Soc.* **2002**, *124*, 11989−11996.
(40) Mallard, W.; Gardner, A. B.; Bass, R.; Slifkin, L. Self-Diffusion in Silver-Gold Solid Solutions. *Phys. Rev.* **1963**, *129*, 617−625.
(41) Doyama, M.; Koehler, J. S. Quenching and Annealing of Lattice Vacancies in Pure Silver. *Phys. Rev.* **1962**, *127*, 21−31.
(42) Simmons, R. O.; Balluffi, R. W. Measurement of Equilibrium Concentrations of Lattice Vacancies in Gold. *Phys. Rev.* **1962**, *125*, 862−872.
(43) Hagel, W.; Westbrook, J. Silver Diffusion in the Intermetallic Compound AgMg. *Trans. TMS-AIME* **1961**, *221*, 951.
(44) Mortlocks, A. J.; Tomlm, D. H. The Atomic Diffusion of Chromium in the Titanium-Chromium System. *Philos. Mag.* **1959**, *4*, 628−643.
(45) Peart, R.; Tomlin, D. Diffusion of Solute Elements in Beta-Titanium. *Acta Metall.* **1962**, *10*, 123−134.
(46) Resing, H.; Nachtmeb, N. Self-Diffusion of Lead, Thallium and Bismuth in the Solid Lead-Thallium System. *J. Phys. Chem. Solids* **1961**, *21*, 40−56.
(47) Guisbiers, G.; Buchaillot, L. Modeling the Melting Enthalpy of Nanomaterials. *J. Phys. Chem. C* **2009**, *113*, 3566−3568.
(48) Guisbiers, G. Size-Dependent Materials Properties Toward a Universal Equation. *Nanoscale Res. Lett.* **2010**, *5*, 1132−1136.
(49) Ye, X.; Zheng, C.; Chen, J.; Gao, Y.; Murray, C. B. Using Binary Surfactant Mixtures To Simultaneously Improve the Dimensional Tunability and Monodispersity in the Seeded Growth of Gold Nanorods. *Nano Lett.* **2013**, *13*, 765−771.
(50) Ravel, B.; Newville, M. *ATHENA, ARTEMIS, HEPHAESTUS*: Data Analysis for X-Ray Absorption Spectroscopy using *IFEFFIT*. *J. Synchrotron Radiat.* **2005**, *12*, 537−541.

DOI: 10.1021/acsnano.8b03978
ACS Nano 2018, 12, 8467−8476